RSC Advances

PAPER

View Article Online
View Journal | View Issue

Check for updates

Cite this: *RSC Adv.*, 2026, **16**, 13548

Improved electron-molecule scattering calculations with the relativistic optical-potential method

Sudhanshu Arya and Bobby Antony *

We present a computational framework for electron–molecule scattering that is intended as a step toward a more accurate and unified description over a broad energy range relevant to applications. The approach combines a spherical complex optical potential (SCOP), constructed from multiconfiguration Dirac–Fock atomic densities *via* a group-additivity scheme, with a partial-wave solution of the Dirac equation. Methane (CH_4) and silane (SiH_4) are used as benchmark targets because of their simple tetrahedral structure and well-documented cross sections. The comparison among exchange models is used to highlight the sensitivity of predicted cross sections to the target model potential and the need for improved model descriptions. In addition, the present Dirac-based implementation is benchmarked against our existing [Joshipura *et al.*, Phys. Rev. A, 2004, 69, 022705] nonrelativistic optical-potential treatment that employs the Numerov method to solve the Schrödinger equation, allowing us to quantify both relativistic kinematic and spinor effects. Although relativistic effects on integral cross sections are minimal, the Dirac treatment has a pronounced impact on the phase shifts and large-angle differential cross sections. Among the exchange models tested, the modified Furness–McCarthy exchange shows the most consistent agreement with benchmark data and represents a clear improvement over our earlier group-additivity SCOP results. This enhancement lays the groundwork for extending the method to larger and strongly polar molecules.

Received 28th January 2026
Accepted 26th February 2026

DOI: 10.1039/d6ra00742b

rsc.li/rsc-advances

Open Access Article. Published on 10 March 2026. Downloaded on 6/15/2026 6:18:40 AM.
This article is licensed under a Creative Commons Attribution-NonCommercial 3.0 Unported Licence.

1 Introduction

Electron collisions with atoms, molecules, and ions sit underneath a lot of the "plumbing" of atmospheric and astrophysical modelling, combustion systems to low-temperature industrial plasmas, and radiation-induced processes in condensed matter and biological systems.[1] In most of these cases, electrons are the main carriers of energy into a medium: they excite, ionise, dissociate, and set up the secondary chemistry that models ultimately aim to track. Cross sections are therefore not merely reported quantities–they are often the indispensable inputs for different plasma-chemistry models, discharge design, planetary-atmosphere simulations, and radiation track-structure calculations.[2] And we need them over a wide energy range, since real electron energy distributions rarely stay politely in one regime. The strong demand for reliable cross-section data has spurred both experimental work and the development of a wide spectrum of theoretical approaches, each with its own strengths and domain of applicability.[3,4]

One persistent complication is that no single theoretical approach is simultaneously reliable and computationally feasible across all energies and targets; consequently, different methods are often adopted in different regimes, making optical-potential approaches a practical route to broad-range cross sections at moderate cost. At low impact energies, roughly below a few tens of electronvolts, exchange must be treated carefully in its exact (non-local) form. The *ab initio* close-coupling methods, such as the *R*-matrix,[5] Schwinger multichannel,[6] and convergent close-coupling[7] methods, are the best choices there. They include exchange and correlation explicitly and resolve narrow resonances and threshold structures with high fidelity. These methods have been applied extensively to small molecules, providing high-accuracy benchmark cross sections in the near-threshold region. But their computational cost scales up rapidly with the number of active electrons, open channels, and number of partial waves, making fully coupled-channel treatments for larger molecules or high energies impractical. At these energies, exchange and correlations become less dominant, and more simplified frameworks become viable, including distorted wave,[8] Born[9] or Born–Bethe[10] approximations and potential-scattering frameworks[11] such as independent-atom and additivity-rule approaches. Additivity rules-based approaches encapsulate the target's many-electron structure into an effective potential that comprises static, exchange, polarisation, and absorptive components; one calculates cross sections for a set of prototype atoms or groups and then constructs molecular cross sections by summing

Atomic and Molecular Physics Laboratory, Department of Physics, Indian Institute of Technology (ISM) Dhanbad, Jharkhand 826004, India. E-mail: bobby@iitism.ac.in

© 2026 The Author(s). Published by the Royal Society of Chemistry

Open Access Article. Published on 10 March 2026. Downloaded on 6/15/2026 6:18:40 AM. This article is licensed under a Creative Commons Attribution-NonCommercial 3.0 Unported Licence.

contributions with suitable geometrical corrections.[12,13] Such methods can produce surprisingly good results at relatively low computational cost, making them attractive for building large cross-section databases.

Among the additivity-based approaches, the independent atom model (IAM) has probably been the most widely used in electron-molecule scattering.[14–17] In IAM the molecular cross section is approximated as a sum of cross sections calculated for isolated atoms treated as independent spherical scatterers located at the nuclear positions. Various refinements, such as screening and interference corrections (IAM–SCAR + I) have been introduced to take into account the shadowing of atoms in the molecule and for coherent multi-centre scattering.[13,18]

A different route is offered by molecular single-centre expansion (SCE)[19] and group-additivity-based optical potential[20] methods. In these approaches, the multi-centre molecular interaction is replaced by an effective central complex potential constructed from a spherically averaged molecular/group density. The spherical complex optical potential (SCOP) model with Hartree–Fock analytic densities[21] has been used successfully across many targets,[22] but implementations have often been purely nonrelativistic. They often treat low- and high-energy collisions with distinct theoretical frameworks. There is still a need for reliable frameworks that can reproduce these data within a single implementation and that can accommodate relativistic effects in a consistent way.

In the present work, we build on this idea by combining (i) group-additivity construction of the target's spherically averaged density derived from multiconfiguration Dirac–Fock (MCDF) atomic densities[23] and (ii) a partial-wave solution of the Dirac equation[24] for the scattering electron. Our emphasis is on method development rather than on generating yet another set of cross sections for a particular molecule. The intent is methodological: to test whether a single Dirac-based SCOP can reproduce benchmark cross sections over a broad energy range while providing a controlled way to assess uncertainties associated with common model ingredients, especially the local exchange approximation. We adopt methane (CH_4) and silane (SiH_4) as benchmark targets because of their tetrahedral symmetry and nonpolar character. Their different sizes and polarisabilities also make them a good probe of model sensitivity.

Methane and silane are the simplest quasi-spherical hydrides. Both are nonpolar, tetrahedral (T_d) molecules consisting of a central heavy atom surrounded by four hydrogens. Methane is widespread in outer-planet atmospheres, combustion, and hydrocarbon plasmas and has been the subject of collision studies for decades.[25–27] Recent investigations highlight its increasing growth rate in Earth's atmosphere, making it an important test molecule. Various cross sections are available across a wide range of energies, including elastic differential, integral, momentum-transfer, total, and ionisation cross sections. Several critical evaluations have produced recommended data sets for these measurements.[28] Silane plays an important role in semiconductor processing. It is a crucial precursor gas in plasma-enhanced chemical vapour deposition (PECVD) and etching of silicon-based materials. Its electron-impact cross sections strongly influence plasma models by controlling radical and ion balance. Total, elastic (including vibrational), and ionisation cross sections have been reported from both experiment and theory,[29–37] albeit not as extensively as for methane. Both targets have been studied theoretically using close-coupling and optical-potential approaches. These studies have revealed low-lying shape resonances, Ramsauer–Townsend (RT) minima, and high-energy behaviours consistent with the Born–Bethe approximation.[25–41]

Although we do not make a direct numerical comparison with IAM-based Dirac treatments[42] here, the present model is intended as a complementary route in which the target structure is incorporated through group additivity rather than independent atoms. Within this framework, an important source of uncertainty lies in the choice of scattering model potentials. For example, different exchange models can lead to noticeable variations in the predicted cross sections, especially near Ramsauer–Townsend minima and low-lying shape resonances. Gianturco and Scialla[43] made this point rather sharply for methane. They showed that the long-range behaviour of approximate exchange outside the static "core" region can control whether the experimentally observed RT minimum appears in the right place, and they proposed a modified semiclassical form that improved agreement with measurements. A systematic comparison of such exchange models within a single SCOP implementation is therefore useful for assessing the sensitivity of the results to the target model potential and for guiding the development of more accurate descriptions. We further compare results obtained with the relativistic Dirac equations to those from an earlier group-additivity SCOP implementation that solves the nonrelativistic Schrödinger equation using the Numerov method.[20,22] Using both modes for these molecules allows us to isolate the effect of (i) static-potential construction, (ii) the selected local exchange model on elastic/total scattering, and (iii) relativistic contributions in light systems. In doing so we aim to position the Dirac SCOP with group-additivity densities as a practical and extendable tool for future work on larger and more complex systems.

The theoretical methods, including the group-additivity potential construction and the Schrödinger/Dirac SCOP formalisms, are outlined in Section 2, while the findings, along with the main comparison between different exchange models and discussions, are presented in Section 3. Section 4 concludes with an outlook for future work.

2 Theoretical methodology

All quantities in this section are expressed in atomic units ($\hbar = m_e = e = 1$) unless explicitly stated otherwise. In these units the speed of light is denoted by $c \approx 137$.

2.1 Target description and spherically averaged MCDF densities

To make the SCOP approach applicable to polyatomic targets without committing to a full single–centre description of the

Open Access Article. Published on 10 March 2026. Downloaded on 6/15/2026 6:18:40 AM.
This article is licensed under a Creative Commons Attribution-NonCommercial 3.0 Unported Licence.

entire molecule, we adopt a group-additivity representation. The molecule is divided into small groups, each consisting of atoms whose charge densities strongly overlap because of covalent bonding. Cross sections are then obtained by summing group cross sections, rather than summing cross sections from fully independent atoms. This idea is related to, but different from, the independent atom model (IAM).[15] In the present group-additivity picture, the basic building blocks remain atomic densities, but they are combined into overlapping fragments and treated as effective scattering centres. In other words, the "independence" assumption is relaxed at the level of how scattering centres are defined. The calculation is not performed atom-by-atom but fragment-by-fragment, with each fragment representing an effectively bonded region where separate atomic contributions are not clearly separable.

For methane and silane, a natural choice is to treat the entire molecule as a single group centred on the carbon or silicon atom, respectively, with all hydrogen atoms included in the group density. In more complex molecules, one might define, for example, CH_3, NH_2, OH, or phenyl groups. This idea is a practical middle ground between a purely IAM-based sum and a single–centre expansion of the molecule. The latter can become increasingly strained as molecular size and anisotropy grow.

The interaction between an incident electron of energy E and a target is modelled by a spherically symmetric complex optical potential $U(r, E)$ centred at a chosen point. In both nonrelativistic and relativistic formulations, we write

$$U(r, E) = V_{st}(r) + V_{ex}(r, E) + V_{ep}(r) + \iota W_{ab}(r, E), \quad (1)$$

where V_{st} is the static potential is, which V_{ex} is a local exchange term, V_{cp} is a correlation–polarization potential, and W_{ab} where the absorptive potential that represents the net effect of all inelastic processes (electronic excitation and ionisation) is.

In the relativistic (Dirac) SCOP, the static potential is built directly from charge densities obtained *via* this group-additivity construction.[22] For each atomic species A ∈ {C, Si, H} we use a spherically averaged electron density $n_A^{(0)}(r_A)$ obtained from MCDF calculations, with r_A measured from the nucleus of atom A, and density normalised to the number of electrons. In the molecule the atomic centres are located at fixed vectors $\mathbf{R}_A$ relative to the group centre. The three-dimensional electronic density of the atom A in the group is approximated as $n_A(\mathbf{r}) = n_A^{(0)}(|\mathbf{r}-\mathbf{R}_A|)$, where $\mathbf{r}$ is measured from the origin. To obtain a central potential, this density is spherically averaged about the origin. For an atom A

$$\bar{n}_A(r) = \frac{1}{4\pi}\int n_A(\boldsymbol{r})\mathrm{d}\Omega_{\hat{r}} = \frac{1}{4\pi}\int n_A^{(0)}(|\boldsymbol{r}-\boldsymbol{R}_A|)\mathrm{d}\Omega_{\hat{r}}, \quad (2)$$

with $r = |\boldsymbol{r}|$, $\mathrm{d}\Omega_r = \sin\theta\,\mathrm{d}\theta\,\mathrm{d}\phi$ and the integral over the direction of $|\boldsymbol{r}|$ at fixed r and R_A (Fig. 1).

Choosing the polar axis along $\mathbf{R}_A$, one has $|\mathbf{r}-\mathbf{R}_A| = \sqrt{r^2 + {R_A}^2 - 2rR_A\cos\theta}$. Writing $u = \cos\theta$, eqn (2) becomes

$$\bar{n}_A(r) = \frac{1}{2}\int_{-1}^{1} n_A^{(0)}\left(\sqrt{r^2 + {R_A}^2 - 2rR_A u}\right)\mathrm{d}u. \quad (3)$$

Equivalently, this average can be expressed as a one-dimensional integral over the radial variable referred to as atom A,

$$\bar{n}_A(r) = \frac{1}{2rR_A}\int_{|r-R_A|}^{r+R_A} n_A^{(0)}(s)s\mathrm{d}s,\ (r>0), \quad (4)$$

with the limiting value $\bar{n}_A(0) = n_A^{(0)}(R_A)$. For atoms placed at the origin ($R_A = 0$) one simply has $\bar{n}_A(r) = n_A^{(0)}(r)$.

The total spherically averaged molecular electron density is then given by the sum over all atoms,

$$\bar{n}_m(r) = \sum_A \bar{n}_A(r), \quad (5)$$

and is normalised to the total number of electrons in the molecule.

$$4\pi\int_0^\infty \bar{n}_m(r)r^2\mathrm{d}r = \sum_A N_A = N_m. \quad (6)$$

To validate this construction, we compared the spherically averaged MCDF-based density with the analytic Hartree–Fock

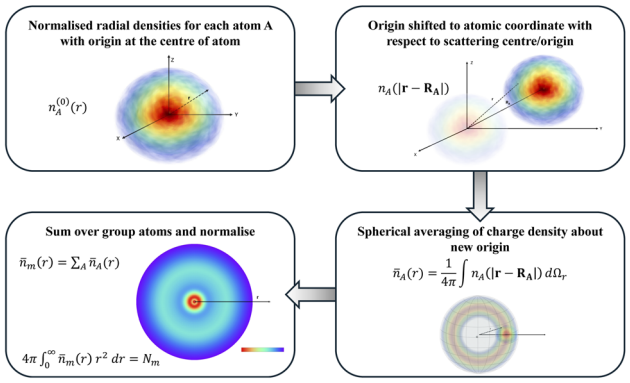

Fig. 1 Schematic of the construction of the spherically averaged target or group electron density.

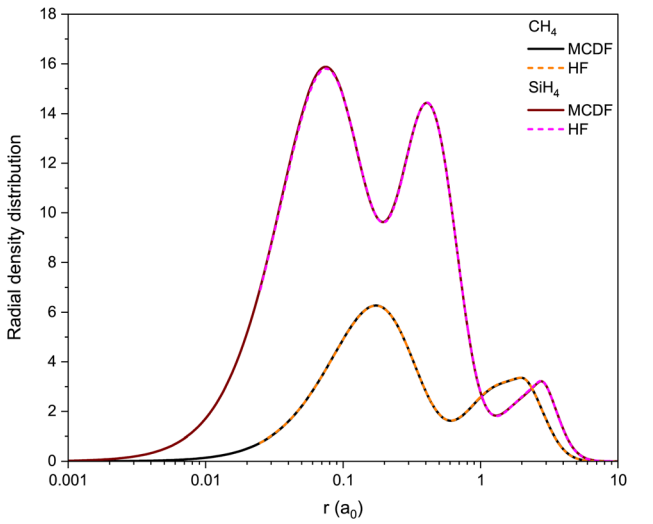

Fig. 2 Radial electron density distribution $4\pi r^2 n(r)$ for methane and silane.

© 2026 The Author(s). Published by the Royal Society of Chemistry

Open Access Article. Published on 10 March 2026. Downloaded on 6/15/2026 6:18:40 AM. This article is licensed under a Creative Commons Attribution-NonCommercial 3.0 Unported Licence.

Yukawa-type parametrisation of Cox and Bonham[21] used in our earlier nonrelativistic SCOP work.[22] Over the radial interval that contributes most strongly to scattering, the two densities are nearly indistinguishable in shape and magnitude. For targets built from relatively light atoms (C, Si, and H), this close agreement is perhaps not too surprising. Fig. 2 illustrates this comparison for methane and silane. Because $\bar{n}_m(r)$ is obtained by spherical averaging about the scattering centre, maxima in Fig. 2 should be interpreted as radial accumulation zones of electron density rather than as signatures of individual orbitals. In CH_4, the first sharp peak at small r originates from the C 1s core, while the second broader peak reflects the valence/bonding region, where C (2s/2p) electrons and the H (1s) densities contribute strongly. In SiH_4, three maxima are resolved because Si exhibits more pronounced shell structure (K-shell and a Ne-like inner core), producing two inner features, whereas the outer peak is dominated by the valence/bonding density together with the hydrogen contributions, which become prominent around the Si–H bond distance. It is important to note that, in the present formulation, the static potential is constructed by evaluating the nuclear and electronic contributions separately, whereas in our earlier nonrelativistic SCOP, both contributions were represented through the analytic Yukawa-type expansions.

2.2 Optical potential from MCDF densities

The static interaction is the sum $V_{st}(r) = V_n(r) + V_e(r)$. The nuclei are treated as point charges at fixed positions. The nuclear contribution to the static potential, spherically averaged about the origin, is

$$V_n(r) = \sum_A \overline{V}_n^{(A)}(r) = \sum_A \begin{cases} -Z_A/R_A, & 0 \le r < R_A, \\ -Z_A/r, & r \ge R_A, \end{cases} \quad (7)$$

where Z_A is the nuclear charge and $R_A = |\mathbf{R}_A|$. The electronic contribution is obtained from the spherically symmetric density *via* the standard radial Coulomb integrals.

$$V_e(r) = -4\pi\left[\frac{1}{r}\int_0^r \bar{n}\left(r'\right)r'^2 dr' + \int_r^\infty \bar{n}\left(r'\right)r' dr'\right]. \quad (8)$$

The local exchange interaction $V_{ex}(r, E)$ is also the focus of the present comparison. We consider three different models built from the spherically averaged density. First, we include Hara's free-electron-gas (HFEG)[44] exchange in exactly the same form as in the Schrödinger SCOP, but evaluated with MCDF-based density $\bar{n}(r)$, to provide the direct link between the two frameworks. Second, we used the semiclassical approximation of Furness–McCarthy,[45] which was designed to reproduce more closely the behaviour of nonlocal exchange interaction in atomic scattering. The third is a modified Furness–McCarthy potential proposed by Gianturco and Scialla,[43] in which the local kinetic energy entering the exchange function is augmented by a correction term

$$\varepsilon_c(r) = \frac{3}{10}\left[3\pi^2\bar{n}(r)\right]^{2/3}, \quad (9)$$

so that an effective kinetic energy

$$T_{eff}(r,E) = T(r,E) + \varepsilon_c(r), \quad (10)$$

are used in constructing the exchange potential. This modification tends to soften exchange in high-density regions and has been reported to improve agreement with experiment.[43] By comparing cross sections computed with HFEG, semiclassical FM exchange, and modified semiclassical exchange (mFM) within the same Dirac SCOP, we can quantify the sensitivity of scattering observables to the choice of local exchange model.

The correlation–polarisation potential $V_{cp}(r, E)$ is taken in the semiempirical form introduced by Zhang *et al.*,[46] which interpolates between a short-range correlation term based on the Perdew–Zunger[47] local-density approximation and a long-range induced-dipole tail.

$$V_{cp}(r) = -\frac{\alpha_d}{2\left(r^2 + r_{co}^2\right)^2}. \quad (11)$$

At large r the potential behaves as $\sim -\alpha_d/2r^4$, where α_d is the molecular dipole polarisability, while at short distances a cut-off r_{co} is used to regularise the r^{-4} singularity and include correlation effects.

The absorption potential $W_{ab}(r, E)$ simulates the net effect of all inelastic processes at a given energy. We adopt a quasifree–scattering picture[48] in which the incident electron undergoes binary collisions with local bound electrons treated as a Fermi gas of density $n(r)$. For energy transfers above an effective threshold I, the probability of inelastic scattering gives rise to a negative imaginary potential W_{ab}. Its functional form is chosen to be consistent with earlier complex optical-potential work; the same absorption model is used in both Dirac and Schrödinger calculations.

2.3 Partial-wave analysis and cross sections

With the complex optical potential of eqn (1), the scattering problem is formulated through the Dirac equation in a central field,

$$[c\boldsymbol{\alpha}\cdot\boldsymbol{p} + \beta c^2 + U(r, E)]\Psi(r) = E\Psi(r), \quad (12)$$

where $\boldsymbol{\alpha}$ and β are the Dirac matrices. Since $U(r, E)$ depends only on r, the solution can be expanded in spinor spherical harmonics labelled by the relativistic quantum number κ and magnetic quantum number m,[49]

$$\Psi_{\kappa m}(r) = \frac{1}{r}\begin{pmatrix} P_\kappa(r)\Omega_{\kappa m}(\hat{\mathbf{r}}) \\ \iota Q_\kappa(r)\Omega_{-\kappa m}(\hat{\mathbf{r}}) \end{pmatrix}, \quad (13)$$

where P_κ (large) and Q_κ (small) component radial functions are the solution of the coupled first-order radial differential equations[49]

$$\frac{dP_\kappa}{dr} = -\frac{\kappa}{r}P_\kappa + \frac{E - U + 2c^2}{c}Q_\kappa, \quad (14a)$$

$$\frac{dQ_\kappa}{dr} = \frac{\kappa}{r}Q_\kappa - \frac{E - U}{c}P_\kappa, \quad (14b)$$

Open Access Article. Published on 10 March 2026. Downloaded on 6/15/2026 6:18:40 AM. This article is licensed under a Creative Commons Attribution-NonCommercial 3.0 Unported Licence.

which we solve numerically using the power-series algorithm of the RADIAL package.[50] At large distances the potential vanishes, and the regular solution behaves as a superposition of incoming and outgoing free Dirac waves. With the usual normalisation, the large component has the asymptotic form[42]

$$P_\kappa(r) \to_{r\to\infty} \sin\left(kr - \ell\frac{\pi}{2} + \delta_\kappa(E)\right), \quad (15)$$

which defines the (generally complex) phase shift $\delta_\kappa(E)$. The corresponding S-matrix element is

$$S_\kappa(E) = \exp[2\imath\delta_\kappa(E)], \quad (16)$$

so that $|S_\kappa| < 1$ whenever the imaginary part of $U(r, E)$ is nonzero and elastic flux is lost to inelastic channels.

The spin-averaged direct and spin-flip scattering amplitudes for a central optical potential can then be written as[14]

$$f(\theta) = \frac{1}{2\imath k}\sum_{\ell=0}^{\infty}[(\ell+1)(S_\ell{}^- - 1) + \ell(S_\ell{}^+ - 1)]P_\ell(\cos\,\theta), \quad (17a)$$

$$g(\theta) = \frac{1}{2\imath k}\sum_{\ell=0}^{\infty}(S_\ell{}^+ - S_\ell{}^-)P_\ell{}^1(\cos\,\theta), \quad (17b)$$

where P_ℓ and $P_\ell{}^1$ are Legendre and associated Legendre functions, and we use the shorthand $S_\ell{}^- \equiv S_{\kappa=-(\ell+1)}$, $S_\ell{}^+ \equiv S_{\kappa=\ell}$.

The spin–averaged elastic differential cross section (DCS) is then

$$\frac{\mathrm{d}\sigma}{\mathrm{d}\Omega} = |f(\theta)|^2 + |g(\theta)|^2. \quad (18)$$

The corresponding integral (elastic) and momentum-transfer cross sections are obtained by angular integration,

$$\sigma_{\mathrm{el}}(E) = 2\pi\int_0^\pi \frac{\mathrm{d}\sigma}{\mathrm{d}\Omega}\sin\,\theta\mathrm{d}\theta, \quad (19a)$$

$$\sigma_{\mathrm{mt}}(E) = 2\pi\int_0^\pi (1-\cos\,\theta)\frac{\mathrm{d}\sigma}{\mathrm{d}\Omega}\sin\,\theta\mathrm{d}\theta. \quad (19b)$$

Grand total cross section is calculated using the optical theorem from the forward scattering amplitude,[51]

$$\sigma_{\mathrm{tot}}(E) = \frac{4\pi}{k}\Im f(0), \quad (20)$$

with k the projectile wave number. The absorption cross section is then defined as the difference

$$\sigma_{\mathrm{abs}}(E) = \sigma_{\mathrm{tot}}(E) - \sigma_{\mathrm{el}}(E), \quad (21)$$

The details of the nonrelativistic SCOP method are given elsewhere.[20,22,52]

3 Results and discussion

In this section all incident energies are expressed in electronvolts (eV) and cross sections in units of 10^{-16} cm^2 (and 10^{-16} cm^2 sr^{-1} for DCS). All the cross sections, for both methane and silane, are computed from the 1–5000 eV range with the same correlation polarisation and absorption potentials. Different exchange corrections (HFEG, FM, and mFM) are compared as mentioned in the previous section.

A point worth keeping in mind throughout is that the integral cross sections (elastic ICS, MTCS, and often TCS) can look "right" even when the DCS is not perfect at some angles because the integral weights can reduce the impact of certain angular regions; large-angle and forward-angle systematics show up differently depending on which integral you look at. This is not just a modelling issue; several experiments also rely on angle extrapolations (especially toward 0° and 180°, so the database itself has built-in sensitivity to that step.

Fig. 3 shows the elastic (integral) and total cross sections for methane calculated with different local exchange models

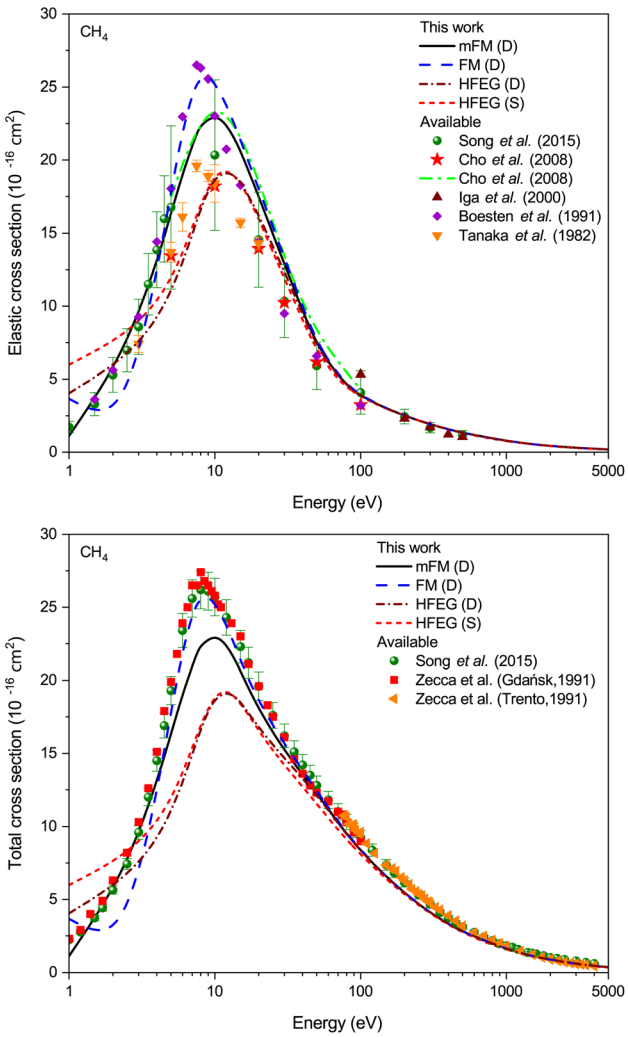

Fig. 3 Elastic (top) and total (bottom) cross sections for electron–CH_4 scattering. Solid, dashed, short-dash-dotted, and short-dashed lines represent Dirac (D) mFM, FM, HFEG, and Schrödinger (S) HEFG exchange calculations, respectively. Available: solid sphere, recommended data of Song *et al.*;[28] star and dash-dotted line, Cho *et al.*;[26] upper-triangle, Iga *et al.*;[27] diamond, Boesten *et al.*;[38] down-triangle, Tanaka *et al.*;[39] square and left-triangle, Zecca *et al.*[40]

© 2026 The Author(s). Published by the Royal Society of Chemistry

Open Access Article. Published on 10 March 2026. Downloaded on 6/15/2026 6:18:40 AM.
This article is licensed under a Creative Commons Attribution-NonCommercial 3.0 Unported Licence.

implemented in the Dirac(D) and Schrödinger(S) SCOP formulations. For methane, the most direct experimental foundation is the family of beam DCS measurements that were later integrated to produce ICS and MTCS. The older benchmark work of Tanaka *et al.*[39] measured elastic DCS in the 3–20 eV range over roughly 30°–140°, and already pointed out a broad peak structure below 10 eV energy consistent with partial-wave behaviour (d-wave dominated region around 7.5 eV). Later, Boesten and Tanaka[38] produced a widely used "reliable standard" dataset for elastic DCS over 1.5–100 eV and 10°–130°, with careful fitting/extrapolation strategies intended to stabilise integral quantities. Their work is part of the reason the community largely shifted away from treating a single early dataset as definitive, because integrals derived from limited-angle DCS were clearly vulnerable to how the extrapolation was done.[26] In the same "mid-energy" window, Curry *et al.*[41] reported absolute elastic DCS for 7.5–20 eV over about 30°–140°, using a crossed-beam spectrometer and normalising their absolute scale to the Tanaka reference strategy (they discussed the normalisation chain explicitly). Cho *et al.*[26] then extended the DCS coverage using a magnetic-angle changer approach to reach 10°–180°, over 5–100 eV, and they are unusually explicit that discrepancies between datasets are often rooted in the extrapolation procedure, especially in the backward hemisphere (120°–180°). Finally, for higher energies, Iga *et al.*[27] measured DCS in 100–500 eV over 10°–135°, noting that the remaining uncertainty in derived integrals is dominated by the angle-extrapolation step. They estimate this contribution at the level of ~tens of percent, depending on energy and which integral you derive.

With that picture in mind, the pattern observed in Fig. 3 is fairly consistent with exchange dominating the low-energy shape and magnitude, and the three models separate cleanly in the low to near-threshold region. In our calculations the mFM curve gives the most reliable overall match, while FM tends to push the elastic strength too high near the maximum, and HFEG tends to sit low in the 10–100 eV region. This is also consistent with the older physical argument emphasised in methane exchange studies.[43] The location and depth of the Ramsauer-type minimum and the low-energy elastic magnitude are highly sensitive to the exchange tail, so a "slightly better" local exchange can matter a lot. The HFEG (D) and HFEG (S) differences at low energies should not be interpreted as relativistic kinematics. The trend mainly reflects the strong near-threshold sensitivity to small phase-shift changes (dominated by a small number of partial waves and is highly sensitive to short-range exchange and interference); small changes in the phase shifts, therefore, translate into noticeable differences in integral cross sections. At higher energies the scattering becomes increasingly perturbative, many partial waves contribute with small phase shifts, and exchange represents a smaller fraction of the interaction; consequently, the Dirac and Schrödinger implementations converge and the HFEG (D) and HFEG (S) curves become nearly indistinguishable.

The elastic ICS and TCS for silane are displayed in Fig. 4. The silane elastic database is thinner than methane. The key experimental DCS set is Tanaka *et al.*,[35] who measured SiH_4 elastic DCS from about 1.8–100 eV over 20°–130°, and then

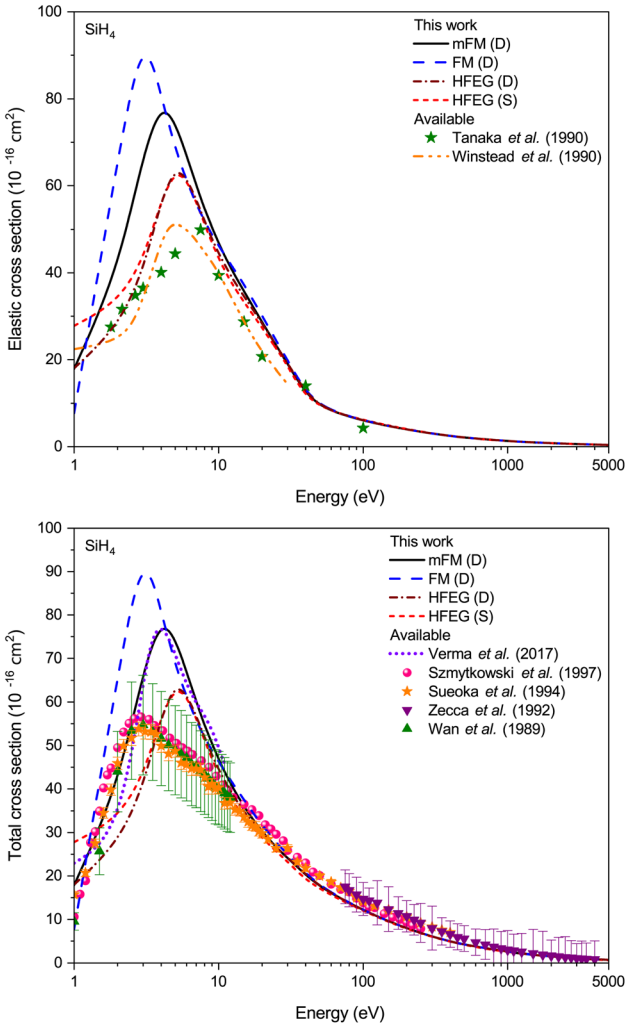

Fig. 4 Elastic (top) and total (bottom) cross sections for electron–SiH_4 scattering. Symbols are the same as Fig. 3, except avilable: dash-dot-dotted line, Winstead *et al.*;[34] olive-star, Tanaka *et al.*;[35] short-dotted line, Verma *et al.*;[30] solid sphere, Szmytkowski *et al.*;[31] orange-star, Sueoka *et al.*;[32] down-triangle, Zecca *et al.*;[33] upper-triangle, Wan *et al.*[53]

derived elastic integrals and MTCS by modified phase-shift fitting to fill in the missing angles. They also emphasised a T_2 shape resonance around ~1.8–2.2 eV, seen in angular distributions and supported by vibrational excitation behaviour.

On the theory side, the static-exchange Schwinger multichannel (SMC) work of Winstead and McKoy[34] is often used as a reference point. They argued that static exchange is "very satisfactory" for silane in roughly the 4–30 eV window but also that below a few eV the missing polarisation physics becomes important. That context matters when interpreting the "SiH_4 *versus* CH_4" difference. Silane is larger and more polarisable, so any local exchange model will be stressed harder at the lowest energies, where correlation–polarisation and exchange compete most strongly. For ECS and TCS, our trends mirror methane but with larger magnitudes, but the same hierarchy emerges. HFEG is typically the lowest, FM is the highest near the peak, and mFM lies in the middle, aligning well with the more recent

© 2026 The Author(s). Published by the Royal Society of Chemistry

Open Access Article. Published on 10 March 2026. Downloaded on 6/15/2026 6:18:40 AM.
This article is licensed under a Creative Commons Attribution-NonCommercial 3.0 Unported Licence.

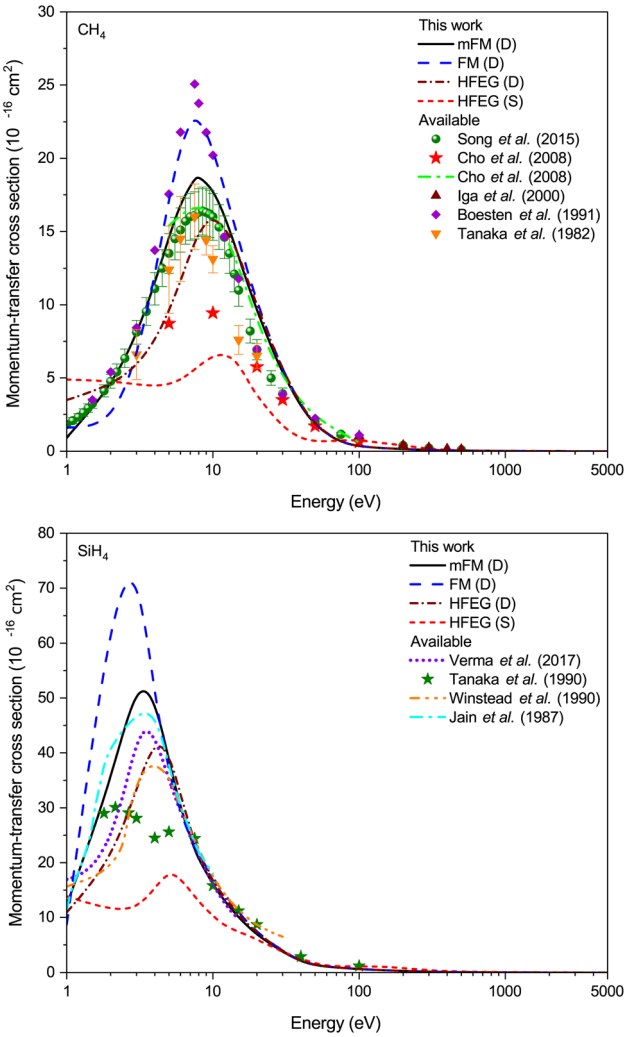

Fig. 5 Momentum-transfer cross sections for methane (top) and silane (bottom). The symbols are the same as in Fig. 3, except available: short-dotted line, Verma *et al.*;[30] olive-star, Tanaka *et al.*;[35] dash-dot-dotted line, Winstead *et al.*;[34] cyan dash-dotted line, Jain *et al.*[37]

theoretical (*R*-matrix) TCS of Verma *et al.*[30] Instead of elastic, the total cross section was more focused for silane, and multiple studies are available, including Wan *et al.*[53] (0.2–12 eV), Szmytkowski *et al.*[31] (0.6–250 eV), Sueoka *et al.*[32] (1–400 eV), and Zecca *et al.*[33] (75–4000 eV). Szmytkowski *et al.*'s work is particularly important because it didn't just show agreement with other available data but highlighted the likely reasons for residual disagreement. They note that transmission experiments can systematically underestimate TCS because of imperfect discrimination of small-angle (forward) scattering, and they explicitly estimate this effect using Tanaka *et al.*'s DCS measurements. They also suggest that magnetic-field usage in some silane TCS experiments may introduce extra systematic uncertainties that are hard to quantify. At the highest energies all curves converge and approach the expected indicating that the details of the static and exchange potentials become less critical once the projectile wavelength is short compared to the molecular size.

Fig. 5 shows the momentum-transfer cross sections (MTCS) for methane and silane. MTCS is where the model differences become harder to hide because of the "angle-sensitive" integral. The $(1 - \cos\theta)$ weighting emphasises angular redistribution rather than just total scattering probability. So, it is often the first place where missing backward scattering or questionable extrapolation shows up. In practice, this makes MTCS both (i) more directly relevant to swarm/transport modelling and (ii) more sensitive to large-angle physics than the elastic integral cross section. In view of the limited coverage of earlier experiments, Cho *et al.*[26] pointed out that disagreements between datasets can often be traced to how the contribution from 120°–180° is treated when deriving MTCS. Song *et al.*[28] highlighted this issue: two Tanaka-based MTCS sets (derived with different spectrometers/normalisations/extrapolations) differ by roughly 30%, so experiments reaching closer to 180° (or with reliable theory-based extrapolation) tend to be more trustworthy. For SiH_4, Tanaka *et al.*[35] provide the main experimental MTCS derived from limited-angle DCS plus phase-shift fitting, and,

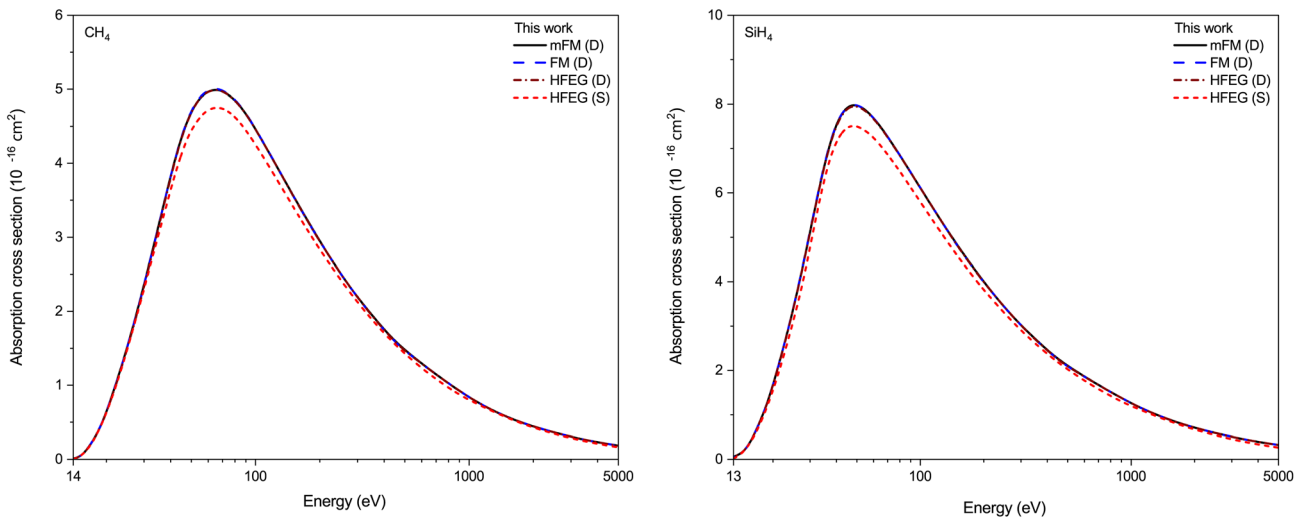

Fig. 6 Absorption cross sections for methane (left) and silane (right). Symbols are the same as Fig. 3.

© 2026 The Author(s). Published by the Royal Society of Chemistry

Open Access Article. Published on 10 March 2026. Downloaded on 6/15/2026 6:18:40 AM.
This article is licensed under a Creative Commons Attribution-NonCommercial 3.0 Unported Licence.

the resonance region makes the MTCS extraction and comparison particularly sensitive. The SMC static-exchange work observed that near the shape resonance, the theory predicts a strong backward enhancement, and they argue that if the experiment does not measure sufficiently far into the backward hemisphere, the integrated and momentum-transfer quantities

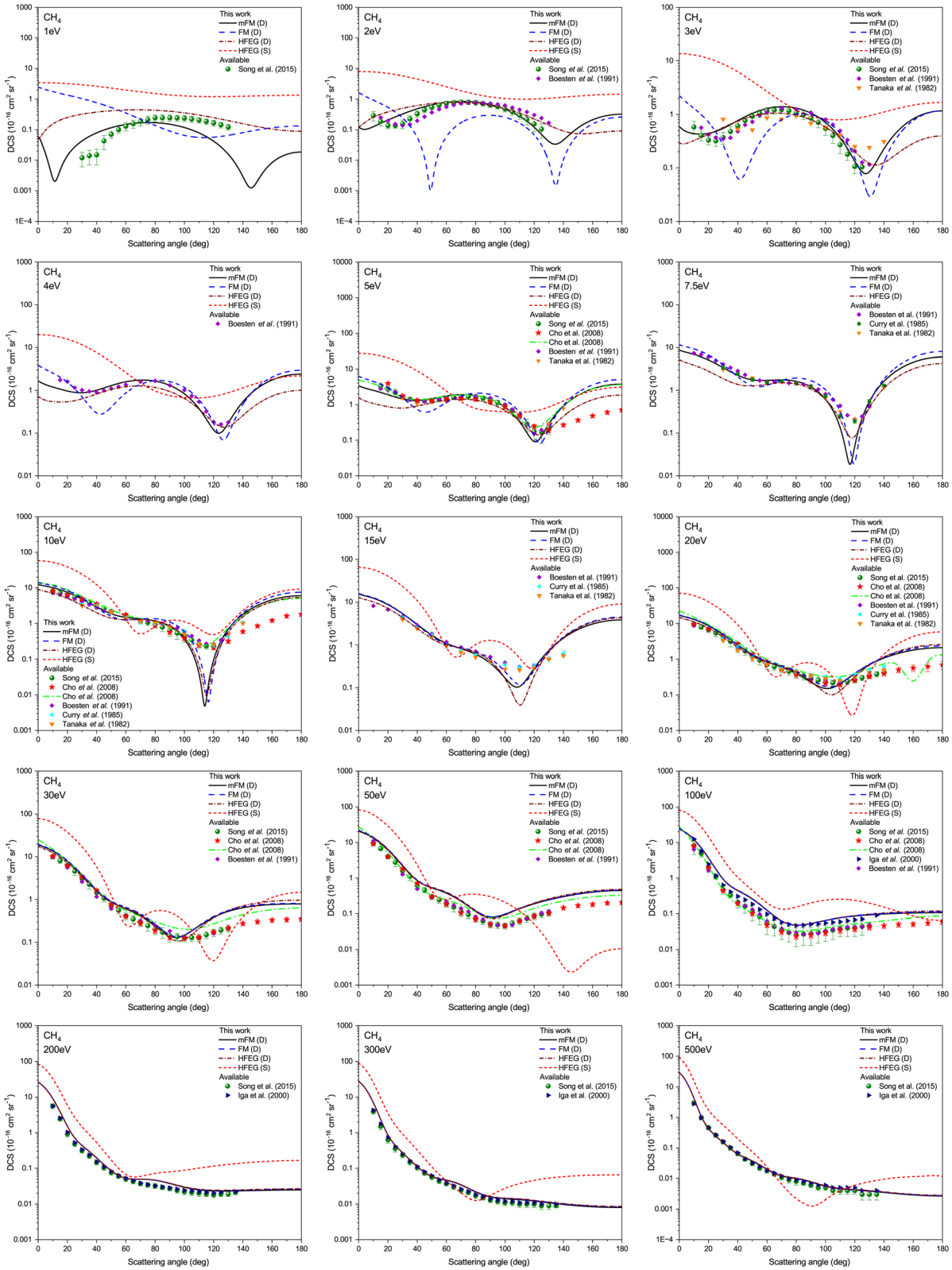

Fig. 7 Elastic DCS for electron–CH_4 scattering at selected energies (as labeled in each panel). The symbols are the same as in Fig. 3, except: left-triangle, Curry *et al.*;[41] right-triangle, Iga *et al.*[27]

Open Access Article. Published on 10 March 2026. Downloaded on 6/15/2026 6:18:40 AM.
This article is licensed under a Creative Commons Attribution-NonCommercial 3.0 Unported Licence.

can be underestimated, and even the apparent resonance peak can shift. In our results, the HFEG (S) model yields the smallest MTCS over the entire energy range and clearly underestimates the measurements in the 3–100 eV region. Dirac mFM consistently improves agreement across the whole energy region. The Dirac implementation helps as well, mainly because it affects phase shifts and therefore the angular distribution, which MTCS "feels" more strongly than ICS does.

The calculated absorption (inelastic) cross-section for both CH_4 and SiH_4, obtained from the optical theorem and eqn (21), is shown in Fig. 6. In our calculations, all four exchange models give very similar absorption curves. A broad maximum of order 5–8 $Å^2$ around 50–70 eV and a slow decrease at higher energies. This insensitivity is expected because the absorption cross-section is dominated by the explicit imaginary part of the optical potential and depends on the elastic channel mainly through the difference $\sigma_{tot} - \sigma_{el}$. Small variations in the elastic

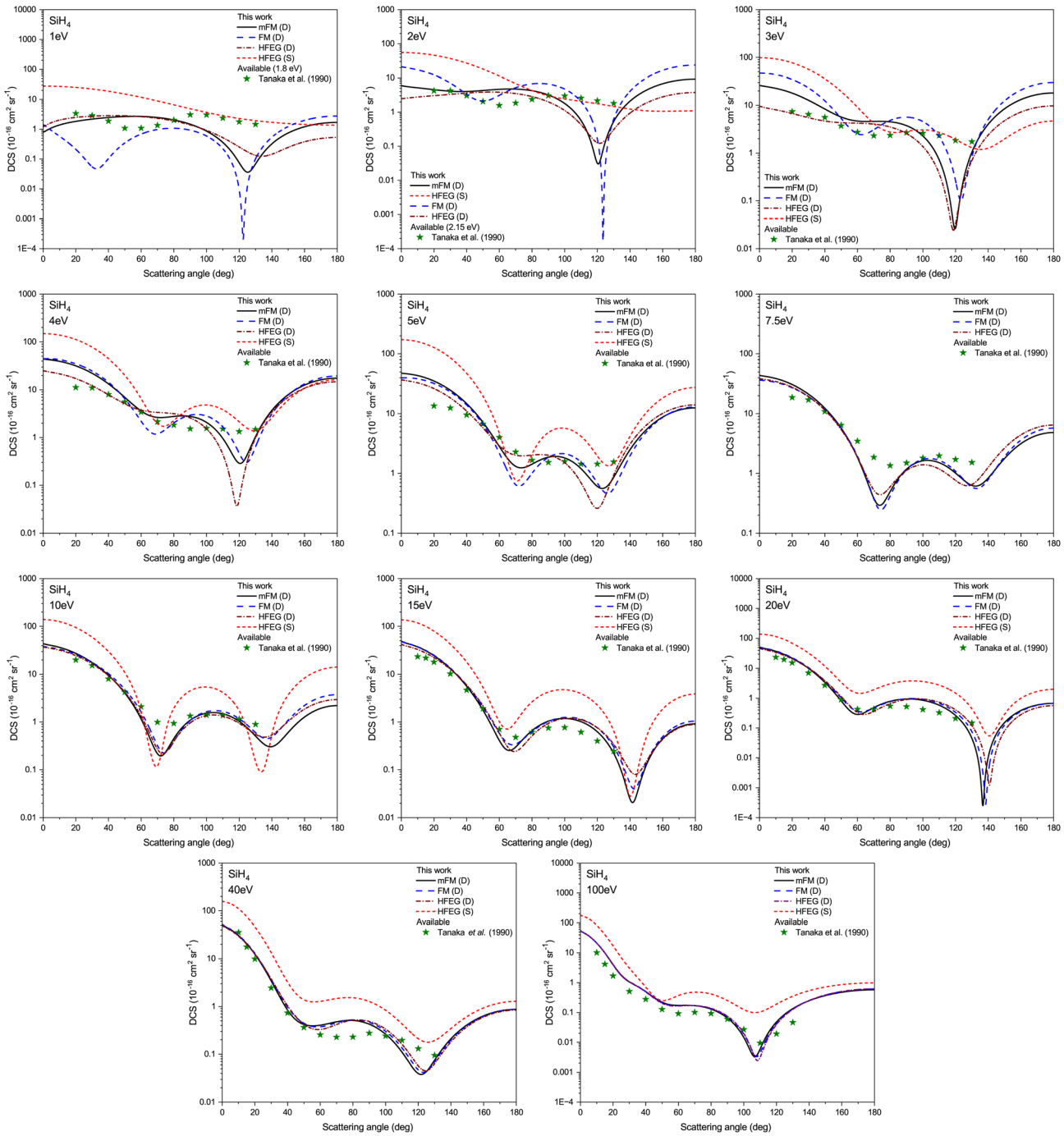

Fig. 8 Elastic differential cross sections for electron–SiH_4 scattering at selected energies (as labelled in each panel). Symbols are the same as Fig. 4. Present calculations are compared with available angular distributions of Tanaka *et al.*[39]

© 2026 The Author(s). Published by the Royal Society of Chemistry

Open Access Article. Published on 10 March 2026. Downloaded on 6/15/2026 6:18:40 AM. This article is licensed under a Creative Commons Attribution-NonCommercial 3.0 Unported Licence.

ICS therefore translate into only modest changes in the absorption cross section.Fig. 7 illustrates the differential cross sections for methane at selected energies (from 1 to 500 eV). The methane DCS literature is dense enough that it helps to think in terms of coveragence. Tanaka[39] and Curry[41] cover mid-angles over 3–20 eV and 7.5–20 eV, respectively, while Boesten & Tanaka[38] extend down to 1.5 eV but still mainly up to 130°. Cho *et al.*[26] pushed to 180°, which is exactly what makes their dataset particularly valuable for pinning down backward scattering. In our methane DCS comparisons, the Dirac implementation tends to improve the large-angle behaviour and the overall angular features, consistent with the general observation that Dirac phase shifts can redistribute intensity into the backward hemisphere. Exchange choice still dominates at the lowest energies, where HFEG (S) calculation significantly overestimates the forward DCS and produces too flat an angular dependence. The mFM (D) usually provides the most balanced agreement across angles. It reproduces the measured angular dependence reasonably well and brings the absolute magnitude closer to the experimental points, although some residual deviation remains below about 3 eV, where details of virtual-state and correlation effects are known to be important.[54] Below a few eV, some mismatch is not surprising even for the best models.The silane DCSs at selected energies between 1 and 100 eV are presented in Fig. 8. Silane DCS comparisons rely heavily on Tanaka *et al.*[35] because they provide the only systematic low-to-intermediate energy angular distributions measurement and explicitly discuss the resonance region. The SMC theory work also matters here, not because it settles the argument, but because it offers a plausible mechanism for experimental underestimation. Strong backward enhancement near resonance may not be fully captured by measurements stopping at 130°. In our silane DCS results, the same hierarchy appears as for methane, with HFEG (S) giving the largest deviation. The Dirac mFM results again provide the closest match to the data. Where discrepancies remain, often around the depth/position of the mid-angle minimum at the lowest energies, suggesting that further refinement of the correlation-polarization or exchange description could be beneficial. From intermediate to higher energies (10 and 100 eV) all Dirac models converge and agree well with the data, whereas the Schrödinger HFEG (S) DCS remains slightly too high at all angles.

Across both molecules and across all observables, the story that emerges is fairly consistent. The exchange model effects are dominant at low and intermediate energies, and mFM is the most consistently successful among the local exchange forms tested. Likely because the density-dependent kinetic-energy correction gives a better low-energy exchange scale than the simpler local energy assumption. The Dirac formulation matters most in the DCS and in the MTCS, both of which are sensitive to phase shifts and large-angle redistribution. While a detailed comparison for other molecules will be presented elsewhere, the present calculations already demonstrate that a single Dirac SCOP with group-additivity densities and an appropriately chosen exchange model can reproduce, within a unified framework, cross sections for two distinct benchmark hydrides from low to high energy. This supports the use of the Dirac SCOP with the modified Furness–McCarthy exchange as a practical starting point for extending the approach to larger, more strongly polar, and chemically more complex molecules.

4 Conclusion

In conclusion, we developed an in-house computer program and benchmarked a computational framework for electron–molecule scattering. In this work we combined a group-additivity SCOP formalism with Dirac partial-wave solutions, and we used methane (CH_4) and silane (SiH_4) as benchmark targets. The resulting elastic and total scattering observables, especially the DCS and MTCS, were compared against available measurements and recommended datasets over a wide energy range. The exchange model effects were observed for both targets in the near-threshold region and in the energy window where the Ramsauer–Townsend minimum and resonance-related structure influence the scattering. Among the exchange models tested, the modified Furness–McCarthy (mFM) model gives the most reliable overall agreement. In the mFM form, the effective kinetic energy entering the exchange function is augmented by a density-dependent correction (for bound-electron contributions that are otherwise neglected). This adjustment appears to be helping in the low-energy region, where small changes in exchange strength and its radial behaviour shift minima and reshape angular structure. But the agreement is not yet perfect, and some mismatches, especially for a higher-Z target, are observed. Two plausible culprits are (i) target-specific density redistributions in the bonding region and (ii) only local density-dependent correlation effects. It is reasonable to say that more accurate (such as density-gradient-dependent) approximations may capture target-specific behaviour more reliably. On the other side, the Dirac-SCOP implementation improved agreement for the DCS and MTCS, which points to better phase-shift estimates. Overall, these refinements suggest that the Dirac-SCOP with the group-additivity rule provides a useful step towards generating cross sections that are not only adequate in totals but also improved in the more demanding observables like DCS and MTCS. Our future direction is to refine the model exchange and correlation terms to incorporate more target-specific physics in the low-energy regime and provide a basis for extending the method to larger and more strongly polar molecules.

Author contributions

Sudhanshu Arya: conceptualisation; data curation; formal analysis; investigation; methodology; software; writing – original draft. Bobby Antony: conceptualisation; resources; supervision; methodology; validation; writing – review & editing.

Conflicts of interest

There are no conflicts to declare.

Open Access Article. Published on 10 March 2026. Downloaded on 6/15/2026 6:18:40 AM. This article is licensed under a Creative Commons Attribution-NonCommercial 3.0 Unported Licence.

Data availability

The data supporting this article have been included as part of the supplementary information (SI). Supplementary information is available. See DOI: https://doi.org/10.1039/d6ra00742b.

Notes and references

1 J. Tennyson, *J. Phys. B: At., Mol. Opt. Phys.*, 2024, **57**, 233001.
2 J. H. Bredehöft, V. Vujčić, D. Jevremović and N. J. Mason, *Atoms*, 2017, **5**(4), 46.
3 M. J. Brunger and S. J. Buckman, *Phys. Rep.*, 2002, **357**, 215–458.
4 K. Bartschat and M. J. Kushner, *Proc. Natl. Acad. Sci. U. S. A.*, 2016, **113**, 7026–7034.
5 J. Tennyson, *Phys. Rep.*, 2010, **491**, 29–76.
6 C. Winstead and V. Mckoy, *Highly Parallel Computational Techniques for Electron-Molecule Collisions*, Academic Press, 1996, vol. 36, pp. 183–219.
7 M. C. Zammit, D. V. Fursa, J. S. Savage and I. Bray, *J. Phys. B: At., Mol. Opt. Phys.*, 2017, **50**, 123001.
8 D. H. Madison and K. Bartschat, in *The Distorted-Wave Method for Elastic Scattering and Atomic Excitation*, ed. K. Bartschat, Springer Berlin Heidelberg, Berlin, Heidelberg, 1996, pp. 65–86.
9 G. C. McCoyd, S. N. Milford and J. J. Wahl, *Phys. Rev.*, 1960, **119**, 149–153.
10 G. García, M. Roteta and F. Manero, *Chem. Phys. Lett.*, 1997, **264**, 589–595.
11 A. Jain, *J. Chem. Phys.*, 1987, **86**, 1289–1300.
12 K. N. Joshipura, B. K. Antony and M. Vinodkumar, *J. Phys. B: At., Mol. Opt. Phys.*, 2002, **35**, 4211.
13 F. Blanco and G. García, *Phys. Lett. A*, 2003, **317**, 458–462.
14 N. F. Mott and H. S. W. Massey, *The Theory of Atomic Collisions*, Clarendon Press, Oxford, 3rd edn, 1971.
15 M. M. Billah, M. M. Khatun, M. H. Khandker, A. K. F. Haque and M. A. Uddin, *Phys. Scr.*, 2024, **100**, 015103.
16 T. Kumer, M. Shorifuddoza, P. K. Das, H. Watabe, M. Shahmohammadi Beni, A. K. F. Haque and M. A. Uddin, *Int. J. Quantum Chem.*, 2025, **125**, e27475.
17 A. I. Lozano, A. García-Abenza, J. Rosado, F. Blanco, J. C. Oller, P. Limão-Vieira and G. García, *Molecules*, 2026, **31**(1), 6.
18 F. Blanco, L. Ellis-Gibbings and G. García, *Chem. Phys. Lett.*, 2016, **645**, 71–75.
19 F. A. Gianturco, D. G. Thompson and A. Jain, in *Electron-Scattering from Polyatomic Molecules Using a Single-Center-Expansion Formulation*, ed. W. M. Huo and F. A. Gianturco, Springer US, Boston, MA, 1995, pp. 75–118.
20 K. N. Joshipura, M. Vinodkumar, C. G. Limbachiya and B. K. Antony, *Phys. Rev. A*, 2004, **69**, 022705.
21 H. L. Cox Jr and R. A. Bonham, *J. Chem. Phys.*, 1967, **47**, 2599–2608.
22 S. Arya and B. Antony, *J. Appl. Phys.*, 2025, **137**, 224903.
23 J. Desclaux, *Comput. Phys. Commun.*, 1975, **9**, 31–45.
24 F. Salvat and R. Mayol, *Comput. Phys. Commun.*, 1991, **62**, 65–79.
25 M. M. Khatun, A. K. F. Haque and M. A. Uddin, *Eur. Phys. J. D*, 2025, **79**, 25.
26 H. Cho, Y. S. Park, E. A. y Castro, G. L. C. de Souza, I. Iga, L. E. Machado, L. M. Brescansin and M.-T. Lee, *J. Phys. B: At., Mol. Opt. Phys.*, 2008, **41**, 045203.
27 I. Iga, M.-T. Lee, M. G. P. Homem, L. E. Machado and L. M. Brescansin, *Phys. Rev. A*, 2000, **61**, 022708.
28 M.-Y. Song, J.-S. Yoon, H. Cho, Y. Itikawa, G. P. Karwasz, V. Kokoouline, Y. Nakamura and J. Tennyson, *J. Phys. Chem. Ref. Data*, 2015, **44**, 023101.
29 D. Mahato, L. Sharma, A. D. Stauffer and R. Srivastava, *Eur. Phys. J. D*, 2019, **73**, 189.
30 P. Verma, J. Kaur and B. Antony, *Phys. Plasmas*, 2017, **24**, 033501.
31 C. Szmytkowski, P. Mozejko and G. Kasperski, *J. Phys. B: At., Mol. Opt. Phys.*, 1997, **30**, 4363.
32 O. Sueoka, S. Mori and A. Hamada, *J. Phys. B: At., Mol. Opt. Phys.*, 1994, **27**, 1453.
33 A. Zecca, G. P. Karwasz and R. S. Brusa, *Phys. Rev. A*, 1992, **45**, 2777–2783.
34 C. Winstead and V. McKoy, *Phys. Rev. A*, 1990, **42**, 5357–5362.
35 H. Tanaka, L. Boesten, H. Sato, M. Kimura, M. A. Dillon and D. Spence, *J. Phys. B: At., Mol. Opt. Phys.*, 1990, **23**, 577.
36 J. Yuan, *J. Phys. B: At., Mol. Opt. Phys.*, 1989, **22**, 2589.
37 A. Jain and D. G. Thompson, *J. Phys. B Atom. Mol. Phys.*, 1987, **20**, 2861.
38 L. Boesten and H. Tanaka, *J. Phys. B: At., Mol. Opt. Phys.*, 1991, **24**, 821.
39 H. Tanaka, T. Okada, L. Boesten, T. Suzuki, T. Yamamoto and M. Kubo, *J. Phys. B Atom. Mol. Phys.*, 1982, **15**, 3305.
40 A. Zecca, G. Karwasz, R. S. Brusa and C. Szmytkowski, *J. Phys. B: At., Mol. Opt. Phys.*, 1991, **24**, 2747.
41 P. J. Curry, W. R. Newell and A. C. H. Smith, *J. Phys. B Atom. Mol. Phys.*, 1985, **18**, 2303.
42 F. Salvat, A. Jablonski and C. J. Powell, *Comput. Phys. Commun.*, 2005, **165**, 157–190.
43 F. A. Gianturco and S. Scialla, *J. Phys. B Atom. Mol. Phys.*, 1987, **20**, 3171.
44 S. Hara, *J. Phys. Soc. Jpn.*, 1967, **22**, 710–718.
45 J. B. Furness and I. E. McCarthy, *J. Phys. B Atom. Mol. Phys.*, 1973, **6**, 2280.
46 X. Zhang, J. Sun and Y. Liu, *J. Phys. B: At., Mol. Opt. Phys.*, 1992, **25**, 1893.
47 J. P. Perdew and A. Zunger, *Phys. Rev. B:Condens. Matter Mater. Phys.*, 1981, **23**, 5048–5079.
48 G. Staszewska, D. W. Schwenke, D. Thirumalai and D. G. Truhlar, *Phys. Rev. A*, 1983, **28**, 2740–2751.
49 M. E. Rose, *Relativistic Electron Theory*, John wiley & Sons, New York, 1961.
50 F. Salvat and J. M. Fernández-Varea, *Comput. Phys. Commun.*, 2019, **240**, 165–177.
51 E. Merzbacher, *Quantum Mechanics*, John wiley & Sons, New York, 2nd edn., 1970.
52 B. Antony, K. Joshipura and N. Mason, *Int. J. Mass Spectrom.*, 2004, **233**, 207–214.
53 H.-X. Wan, J. H. Moore and J. A. Tossell, *J. Chem. Phys.*, 1989, **91**, 7340–7347.
54 J. Tennyson, *Phys. Rep.*, 2010, **491**, 29–76.

© 2026 The Author(s). Published by the Royal Society of Chemistry